Nanoscale

PAPER

View Article Online
View Journal

Cite this: DOI: 10.1039/c9nr01395d

Intracellular dynamics of superparamagnetic iron oxide nanoparticles for magnetic particle imaging

Eric Teeman, [a] Carolyn Shasha, [b] James E. Evans[c] and Kannan M. Krishnan*[a,b]

Received 14th February 2019,
Accepted 20th March 2019

DOI: 10.1039/c9nr01395d

rsc.li/nanoscale

Superparamagnetic iron oxide nanoparticles (SPIONs) are a foundational platform for a variety of biomedical applications. Of particular interest is Magnetic Particle Imaging (MPI), which is a growing area of research and development due to its advantages including high resolution and sensitivity with positive contrast. There has been significant work in the area of *in vivo* optimization of SPIONs for MPI as well as their biodistribution in and clearance from the body. However, little is known about the dynamics of SPIONs following cellular internalization which may limit their usefulness in a variety of potential imaging and treatment applications. This work shows a clear 20% decrease in magnetic performance of SPIONs, as observed by Magnetic Particle Spectroscopy (MPS), after internalization and systematic consideration of applicable factors that affect SPION signal generation, including microstructure, environment, and interparticle interactions. There is no observed change to SPION microstructure after internalization, and the surrounding environment plays little to no role in magnetic response for the SPIONs studied here. Interparticle interactions described by dipole–dipole coupling of SPIONs held close to one another after internalization are shown to be the dominant cause of decreased magnetic performance in cells. These conclusions were drawn from transmission electron microscopy (TEM) image analysis at relevant length scales, experimentally prepared and characterized SPIONs in varied environmental conditions, and theoretical modeling with Monte Carlo simulations.

Introduction

Biomedical imaging[1] is central to understanding biological processes as well as disease management from diagnosis to staging, treatment planning, and monitoring the efficacy of treatment. Current clinical imaging modalities include angiography, molecular imaging of cancer,[2] and stem cell-based therapies.[3] Magnetic Particle Imaging[4] (MPI), the first completely new imaging method in nanomedicine to emerge in the last three decades, offers the potential of being an ideal *in vivo* tomographic imaging modality with demonstrated preclinical applications that include real-time perfusion imaging in acute stroke,[5] cancer detection,[6] stem-cell tracking,[7,8] gut-bleed detection,[9] angiography, and blood-pool imaging.[10–12]

MPI is a tracer-based modality that directly images superparamagnetic iron oxide nanoparticles (SPIONs),[13] with signal intensity and resolution critically dependent on their *in vivo* relaxation dynamics.[14] As such, MPI offers high image contrast (with negligible background signal from diamagnetic tissue), a signal linear with tracer concentration[15] and zero depth attenuation, and is safe as it uses no ionizing radiation. Additionally, a demonstrated high sensitivity (200 nM Fe)[16] and high temporal resolution[17] is achieved when optimized SPIONs of tailored size and size dispersity are used.[18,19] Overall MPI promises a biomedical imaging modality that combines the speed of X-ray computed tomography (CT), the safety of magnetic resonance imaging (MRI), and the sensitivity of positron-emission tomography (PET). Almost all these recent advances in MPI, especially in the context of clinical translations, are critically dependent on the *in vivo* magnetic relaxation behavior and pharmacokinetics[20] of the SPION tracers. Much progress in MPI has been accomplished by the optimization of SPION cores, including their size and size distribution, iron oxide phase purity and crystallinity,[21] as well as their colloidal characteristics, such as their hydrodynamic size, zeta potential, surface hydrophobicity, and surface functionalization. However, further developments in MPI, particularly the translational applications for cardiovascular disease, molecular imaging of cancer, and stem-cell tracking, requires a detailed understanding of the biological fate of the SPIONs, their interactions with cells, and the effects of these interactions on MPI signal, especially in the *in vivo* environment.

When SPIONS are delivered *via* injection into the bloodstream, they are exposed to a complex mixture of serum

[a]Department of Materials Science & Engineering, University of Washington, Seattle, WA 98195, USA. E-mail: kannanmk@uw.edu
[b]Department of Physics, University of Washington, Seattle, WA 98195, USA
[c]Environmental Molecular Sciences Laboratory, 3335 Innovation Boulevard, Richland, WA 99354, USA

proteins, and these extracellular serum proteins adsorb onto the SPION surface forming a protein corona.[22] Protein adsorption is driven by hydrophobic and electrostatic interactions, combined with the increase in entropy as the protein unfolds when bound on the curved SPION surface.[23] This protein corona, comprising largely of albumin and some lower abundance proteins (immunoglobulins, apolipoproteins, fibrinogen, *etc.*),[24] determines the nanoparticle stability, cellular binding, and cellular internalization.[25] However, a polymer brush coating, *e.g.* a neutral polymer such as polyethylene glycol (PEG), can reduce protein adsorption by generating steric forces; both the brush surface density and the polymer molecular weight are important parameters.[26] Indeed, the SPIONs used in prior work leading up to this study were optimally loaded (18.8%) with a high molecular weight (20 kDa) PEG and show long-term systemic retention in mice and are promising blood-pool agents for MPI imaging in cardio- and cerebrovascular disease models.[2,9] Delivery of these long-circulating SPIONS to the leaky tumor vasculature of a breast xenograft mice model by the enhanced permeation and retention mechanism[27] has been used to demonstrate[3] MPI as an *in vivo* imaging platform for cancer detection.

The logical question that follows relates to what the cellular fate is of these SPIONS that are being optimized for *in vivo* applications in MPI. Magnetic relaxation physics dictates that the SPIONS be 23 to 28 nm in core diameter for best MPI resolution and signal intensity. Coincidentally, theoretical considerations[28] based on membrane deformation result in models that also converge on the same conclusion: particles have to have a minimum hydrodynamic diameter of 40 to 60 nm to achieve cellular uptake by endocytosis.[29] While a large amount of work[30] has been devoted to studying endocytosis of SPIONs, only a minimal understanding has been obtained on their fate after they enter the cells.[31] It is known that the SPIONs reside in membrane-bounded vesicles,[32] or endosomes, right after endocytosis; however, the ramification of the intracellular fate of SPIONS on their magnetic relaxation dynamics and the MPI signal is an open question. In this paper, we address this critical question by combining experiment and Monte Carlo simulations and provide crucial insight relevant to the future development of MPI as a viable cell-tracking imaging modality.

Experimental

Core synthesis

The SPIONs used in this work were prepared based on previously published methods.[21,33] Briefly, a solution of iron(III) chloride and sodium oleate were dissolved in a mixture of hexanes, ethanol, and water (liquid ratio 5 : 3 : 1.8). In a flask equipped with a cooled condensing column, this mixture was heated for 4 h at reflux (57 °C). The resultant iron oleate product was washed three times and extracted in a separatory funnel. The organic phase was collected, dried with sodium sulfate, and filtered with qualitative filter paper. The solvent was removed first by careful rotary evaporation, then by vacuum for at least 2 h.

Based on determined mass after solvent removal, iron oleate was diluted to the appropriate concentration with 1-octadecene and oleic acid. The reaction mixture was placed under vacuum and heated at 50 °C overnight. Two bump bulbs were added to the reaction flask and the system purged by vacuum and argon gas. Under an inert atmosphere, the temperature was brought to 324 °C and held until nucleation occurred (observed as a color change to white brown) plus 15 min. The temperature was then lowered to 318 °C and a 1% oxygen/99% argon gas flow was added. The reaction was held in this state until 39 h had passed since the initial point of nucleation.

Characterization of the size, size distribution, and crystallographic phase was carried out by Transmission Electron Microscopy (TEM). TEM samples are prepared on 200 mesh pure carbon-coated copper grids by depositing 2 μL of 1 mg mL^{-1} nanoparticle solution in chloroform on the carbon surface and allowed to air-dry. Sizes and size distribution are determined using ImageJ and histograms fitted with a log-normal distribution.

Polymer synthesis

As synthesized SPIONs were made hydrophilic through the addition of amphiphilic polymer coatings. Briefly, poly(maleic anhydride-*alt*-1-octadecene) (PMAO) and amine-terminated polyethylene glycol (PEG) were each added to solutions of dichloromethane (DCM) and small amounts of triethylamine (Et_3N), allowed to dissolve fully; then the solutions were combined in one container. The reaction was allowed to proceed for 48 h and the viscosity of the solution was observed for signs of reaction progress.

The resulting copolymer was dried by rotary evaporation, placed under vacuum for several days, and then dissolved in deionized water. The new solution was transferred to 100 kDa cutoff tubing and put in a beaker with deionized water. The water was replaced several times over two to three days and the purified product was transferred to a round-bottom flask. The solution was frozen in an acetone and dry ice bath while spinning at 300 rpm. The copolymer was lyophilized over four days and the final product collected and weighed. It was then stored under vacuum or inert gas until used in the SPION coating process.

Phase transfer

SPIONs were transferred to aqueous solution following adaptation of previous methods.[34,35] SPIONs were washed in different solvent mixtures to remove synthesis by-products and excess reaction solvent and surfactant. The solvent mixtures were ethyl acetate (100%) once, hexanes and ethyl acetate (50%/50%) once, and hexanes/acetone (40%/60%) five times. Each solvent mixture was added and the sonicated with the SPIONs for 30 to 60 s. The container was then placed on a strong magnet until the SPIONs had entirely moved in solution to be adjacent to the magnet. The supernatant was then

removed by pipette and the next solvent mixture added. After the final removal of solvent, the SPIONs were placed under vacuum for approximately of 24 h.

The dried SPIONs were weighed and chloroform added to a concentration of 1 mg mL^{-1}. Amphiphilic polymer was then added in a ratio of 10 mg per 1 mg SPIONs and allowed to dissolve overnight while on a shaker table. The solvent was then removed by rotary evaporation, leaving behind a film of SPIONs and polymer coating the container. This was dried under vacuum for 24 h followed by the addition of deionized water to a concentration of 1 mg mL^{-1}. The new solution was sonicated for approximately 3 h and the hydrodynamic size checked by Dynamic Light Scattering (DLS). The SPIONs were transferred to 1× PBS by gel chromatography in a PD-10 column equilibrated in 1× PBS. The final concentration of the solution was determined through elemental analysis by inductively coupled plasma optical emission spectrometry (ICP-OES). SPIONs in aqueous solution were stored at 4 °C until ready for use.

Cell culture and SPION exposure

Human epithelial fibrosarcoma cells (HT-1080) were maintained in Eagle's Minimum Essential Medium (EMEM) supplemented with 10% FBS and 1% penicillin–streptomycin at 37 °C and 5% CO_2 atmosphere. Cells were passaged at least three times after thawing before use and never allowed to reach higher than 90% confluence. SPIONs were made sterile through 200 μm filtration and diluted down to the necessary concentration using 1× PBS. SPION solutions were then diluted to final exposure concentration with EMEM supplemented with 1% penicillin–streptomycin. All solutions had equal total volumes and percentage of media; only SPION concentration was varied.

Cells were seeded in 6-well plates at 3×10^6 cells per well in 3 mL of media and maintained for 24 h at 37 °C and 5% CO_2 atmosphere. Media was then aspirated off, cells washed with 1× PBS, and media containing SPIONs added to the wells. Exposure was allowed to continue for 24 h, then the supernatant was aspirated off, cells washed with 1× PBS, and cells collected with 0.25% Trypsin-EDTA. The cells were then spun down at 1000 rcf for 5 min, the supernatant removed, and 100 μL fresh media added.

Magnetic particle spectroscopy

All SPION samples were analyzed using a home-built spectrometer[36] with a drive frequency, f_0, of 26 kHz and a maximum field amplitude, H_{max}, of 20 mT. All measurements were repeated three times and the acquired signal averaged. Before measurement, iron concentration of each sample was determined while in the liquid state using an Inductively Coupled Plasma-Optical Emission Spectrophotometer (ICP-OES; PerkinElmer Optima 8300). Samples were digested in concentrated HCl and diluted 1000-fold in deionized water prior to analysis. Concentrations were interpolated from a linear fit of measured standard concentrations ($R^2 > 0.999$).

150 μL of SPIONs dispersed in aqueous media were transferred to individual tubes for measurement by MPS. Samples containing cells exposed to SPIONs were maintained in culture media of no more than 100 μL previously ensuring that media did not produce any MPS signal. Immobilized samples were prepared initially with 150 μL of SPION dispersion transferred to individual tubes to maintain consistency with liquid samples, then frozen through immersion in liquid nitrogen and lyophilized at approximately −60 °C and 6 mTorr. Any physical changes of dried matrices were noted to ensure sample remained within the appropriate region for detection in the MPS pick-up coil.

Fluorescence and electron microscopy

Samples were prepared for electron and confocal fluorescence microscopy following the same cell exposure procedure as stated above. Three wells were seeded with coverslips on the bottom to allow for confocal microscopy. After 24 h of incubation, the supernatant was aspirated and serum-free media added. Two drops of NucBlue fluorescent dye was added to each well and allowed to sit at room temperature for 20 min. This mix was then aspirated away, cells gently washed with 1× PBS, and coverslips were transferred to a new well plate with 4% paraformaldehyde that had been prepared fresh in 1× PBS and 0.03 M sodium cacodylate. This was incubated at room temperature for 20 min while protected from light. The paraformaldehyde solution was aspirated, coverslips washed with 1× PBS twice, and mounted to microscope slides using one drop of Vectashield mounting medium. Samples were stored for no more than one day at 4 °C before imaging. Confocal fluorescence microscopy was performed using a Leica DMi8 (Leica Microsystems GmbH, Germany) inverted confocal microscope with 405, 488, 532 nm excitation lasers and PMTs corresponding to fluorophore emission peaks to avoid spectral overlap and allow simultaneous multicolor imaging.

To the remaining culture plate wells, without coverslips initially, 0.25% Trypsin-EDTA was added. Released cells were collected in centrifuge tubes, pelleted, and supernatant was removed. 100 μL of pre-melted 1% low-melting-point agarose was added and the mixture spun down at 1500 rcf for 10 min. Tubes were cooled at 4 °C for 30 min to solidify the agarose solution, after which 1 mL of Karnovsky's fixative was added. Samples were kept at 10 °C and shaken at 300 rpm overnight. Samples were then stained in 1% osmium tetroxide for 3 h. Agarose blocks were trimmed to remove excess not containing cells, noted by a lack of blackened color from osmium cell staining. The cell-containing agarose blocks were then dehydrated in the following ratios of acetone and Milli-Q water; 50 : 50, 70 : 30, 90 : 10, 100 : 0, 100 : 0. Samples were embedded in PolyBed/Araldite resin following a dilution series of increasing resin and decreasing acetone at each step in the following ratios; 33 : 67, 50 : 50, 67 : 33, 100 : 0. The resin was cured at approximately 65 °C for five days.

Resin blocks were trimmed with razor blades until cells were near the resin block surface and ultra-thin sectioned using a diamond knife to 70 nm thick. Serial-sections were col-

lected where possible, with the priority being consistent section coloring. Sections were adhered to 75 mesh Cu TEM grids coated with pure carbon and Formvar. Samples were post-stained with 2.5% Uranyl Acetate Alternative (Ted Pella, Inc.; Gadolinium Triacetate) for 8 min and 0.1% Lead Citrate solution for 90 s. Bright-field imaging was carried out using a JEOL JEM-3000SFF (JEOL USA, Inc., Peabody, MA) transmission electron microscope with a direct electron detector and operated at 300 kV. Scanning probe imaging was carried out using an FEI Titan 80-300™ with a Gatan CCD camera and operated at 300 kV.

Monte carlo simulation

SPIONs under an applied magnetic field will have some magnetization defined, in the equilibrium case, by the Langevin function.[13] Here it is assumed that equilibrium occurs when $\tau \ll 1/f$ where τ is the relaxation time and f is the magnetic field frequency. MPI employs frequencies greater than several kHz where the equilibrium approximation is no longer valid. The non-zero relaxation time results in a phase-lag of magnetic nanoparticle alignment with the applied field, which varies between different core sizes in real-world samples with a distribution of core sizes. The overall effect of non-zero relaxation times in MPI is a decrease in resolution.

It is important to understand the relaxation mechanisms by which magnetic nanoparticles align with an applied field to fully characterize deviations from ideal performance under a given applied field and frequency. The two mechanisms are Brownian[37] and Néel[38] relaxation which are different methods of moving the magnetic moment within a particle by physical rotation of the particle and internal rotation of the moment itself, respectively. These mechanisms are both available to nanoparticles in liquid and thus both must be considered when describing the dynamics of nanoparticles under an applied field with relatively high frequencies. To more accurately characterize the behavior of SPIONs, then, we utilize Monte Carlo simulations on nonlinear dynamics. The implementation used in this work has been validated previously against experimental conditions.[39] In brief, combined stochastic differential equations are solved to determine the magnetization direction based on internal magnetization,

$$\frac{d\mathbf{m}}{dt} = \frac{\gamma}{1+\alpha^2}(\mathbf{H} + \alpha\mathbf{m} \times \mathbf{H}) \times \mathbf{m} \quad (1)$$

where $\mathbf{m}$ is a vector describing the magnetization, $\mathbf{H}$ is the effective magnetic field, γ is the electron gyromagnetic ratio, and α is the damping coefficient. The second equation describes the physical dynamics,

$$\frac{d\mathbf{n}}{dt} = \frac{\boldsymbol{\theta}}{6\eta V_h} \times \mathbf{n} \quad (2)$$

where $\mathbf{n}$ is a vector describing the easy axis, $\boldsymbol{\theta}$ is the effective torque, η is the solution viscosity, and V_h is the hydrodynamic volume. These equations are unit vectors and describe direction while the magnitude of the magnetic moment is defined by the saturation magnetization, M_s times the volume of the nanoparticle core, V_c.

In this model, additional considerations are made for thermal fluctuations by assuming a Gaussian stochastic process effectively describes the nanoparticle movement at a given temperature.[39] In addition, under normal operation, dipolar interactions between magnetic nanoparticles are ignored by assuming they will be sufficiently dispersed in a liquid environment to be non-interacting. In the more compact space within a cell it is possible for nanoparticles to be held in close proximity; thus magnetostatic interactions have been taken into account in this work by incorporating the change in total energy from dipolar coupling between all particles.

Results & discussion

Three separate batches of SPIONs have been synthesized The sizes and magnetic properties of these particles have been characterized before use by TEM, VSM, and MPS and are shown in Fig. 1. The SPIONs show increasing core diameters and narrow size distribution parameters of 21.9 (0.04), 25.3 (0.08) and 27.8 (0.06) nm (σ) and are approaching optimal performance in MPI. There is some overlap in size for these batches as illustrated by the histograms in Fig. 1a. These SPIONs show expected MPS properties as core diameter increases including increasing peak intensity, narrowing FWHM, shown in Fig. 1c, and slower loss in amplitude with increasing harmonic number, shown in Fig. 1d. Note that the FWHM of the point spread function (PSF) is correlated with the rate of amplitude loss with increasing harmonic in the harmonic distribution where narrower FWHM equates to slower amplitude loss. Deviation from the expected trend is observed by VSM in Fig. 1b where the largest core diameter, 27.8 nm, shows a lower saturation magnetization than the next largest, 25.3 nm. This is attributed to increased agglomeration during the phase transfer process resulting in a small fraction of SPIONs in this sample acting as multicore particles with dipolar interactions between cores. This is also observed by the small shoulder in Fig. 1c for the 27.8 nm sample.

Once SPIONs were suitably characterized, they were exposed to epithelial cancer cells with the goal of observing their magnetic performance by MPS and determining if any changes result. Environmental conditions present within cells and known physical properties of magnetic materials were used to dictate intracellular performance. Each of these factors is experimentally and theoretically controlled for direct comparison to cell internalized SPION counterparts.

SPION uptake into cells is dependent on the particle coating characteristics including PEG chain length, loading percentage of PEG chains per PMAO backbone chain, and surface charge. Previous work[12] helped identify the optimal combination of these characteristics for long-circulation, but to promote cell internalization, the PEG loading percentage has been decreased to 3–5% for this work with resulting

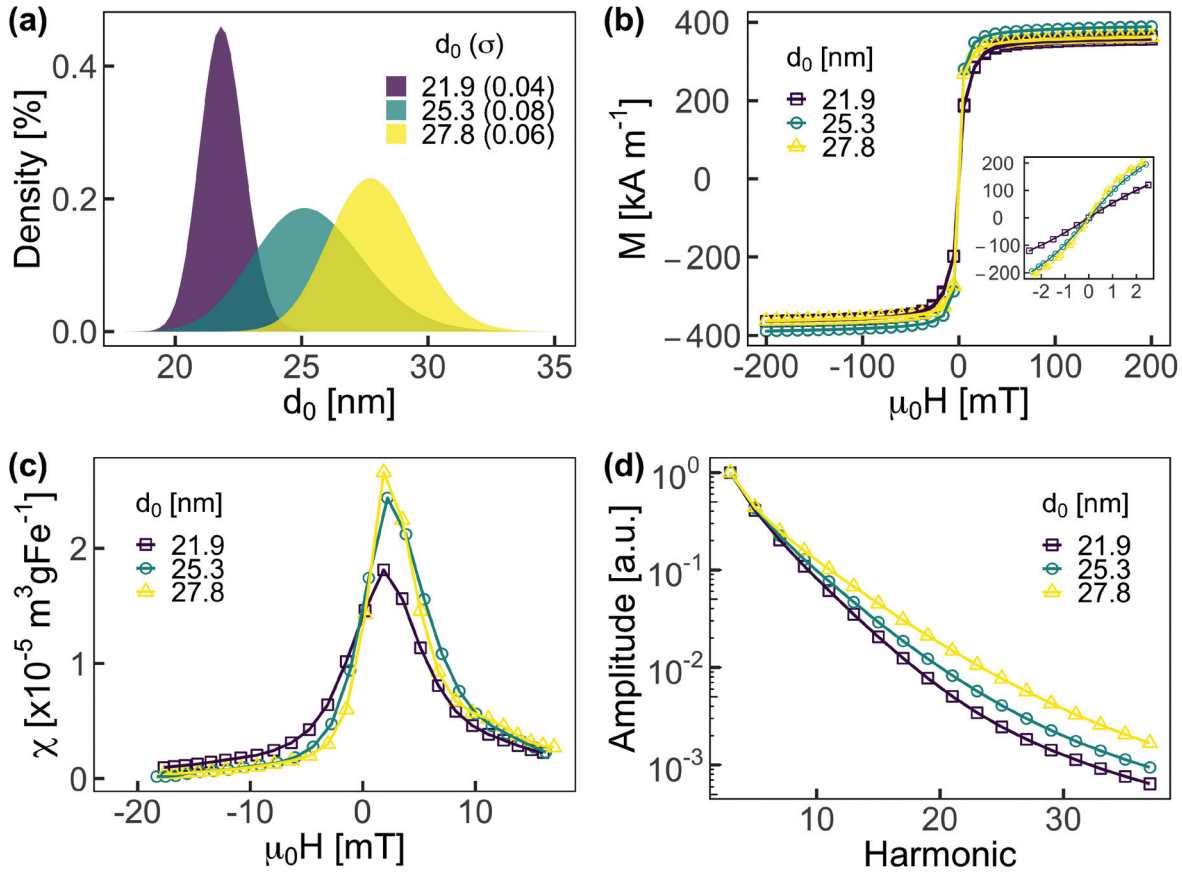

Fig. 1 Initial characterization of SPIONs used in this work by TEM for the determination of size and size distribution (a), VSM to confirm superparamagnetic hysteresis and saturation magnetization (b), and MPS as a substitute for direct MPI imaging performance including the point spread function (c) and harmonic distribution (d).

increased surface charge per particle. The 20 kDa PEG chain molecular weight has been held constant from previous work to maintain most or all of the magnetic performance.

SPIONs coated with PMAO–PEG and incubated with HT-1080 epithelial cancer cells are readily observed to show uptake by quantification of iron content in cells (not shown here), but their localization exterior or interior to the cell is unknown by that method. Nanoparticles will experience significantly different environments based on their localization. For example, media and serum containing salts, sugars, and proteins exist outside of the cell membrane, and these components are capable of adhering to the nanoparticles thereby potentially changing their hydrodynamic size or causing electrostatic agglomeration that may prevent uptake. Inside the cell, the nanoparticle will experience increased viscosity of cytoplasm and organelles and decreased pH within lysosomes,[40,41] to name a brief subset of possible conditions.

Particle localization in imaging is first established through confocal microscopy of cells with fluorescent dye-labeled nuclei and exposed to dye-conjugated SPIONs. *Z*-projections of cells both non-exposed, Fig. 2a, and exposed, Fig. 2b, to SPIONs illustrate significant uptake. Individual organelles are visible as locally concentrated higher intensity fluorescent signal as compared to surrounding cellular material suggesting the highest concentration of labeled SPIONs are present in these vesicles. It is not possible to discern the vesicle type through these images and magnifications nor do they unambiguously confirm internalization *vs.* adherence to the cell surface of SPIONs. Thus, further investigation has been carried out through the use of TEM imaging of cells both without, Fig. 2c, and with, Fig. 2d, internalized SPIONs. These images confirm localization of SPIONs only within cytoplasmic vesicles. Higher magnification imaging further confirms that these vesicles are endosomes, shown in Fig. 2e, and lysosomes, shown in Fig. 2f, as is expected for uptake of nanoparticles through endocytosis pathways and in agreement with prior observations of PEG-coated SPIONs.[8]

SPIONs being found only in endosomes and lysosomes provides a small number of potential mechanisms through which changing magnetic performance can occur after internalization in cells. The first mechanism to consider a change in the average core size and size distribution of the SPIONs after internalization. Both of these characteristics are key to the relaxation dynamics and resulting relaxation times of magnetic nanoparticles[42,43] and there is potential for the environment within lysosomes to affect them after extended incubation

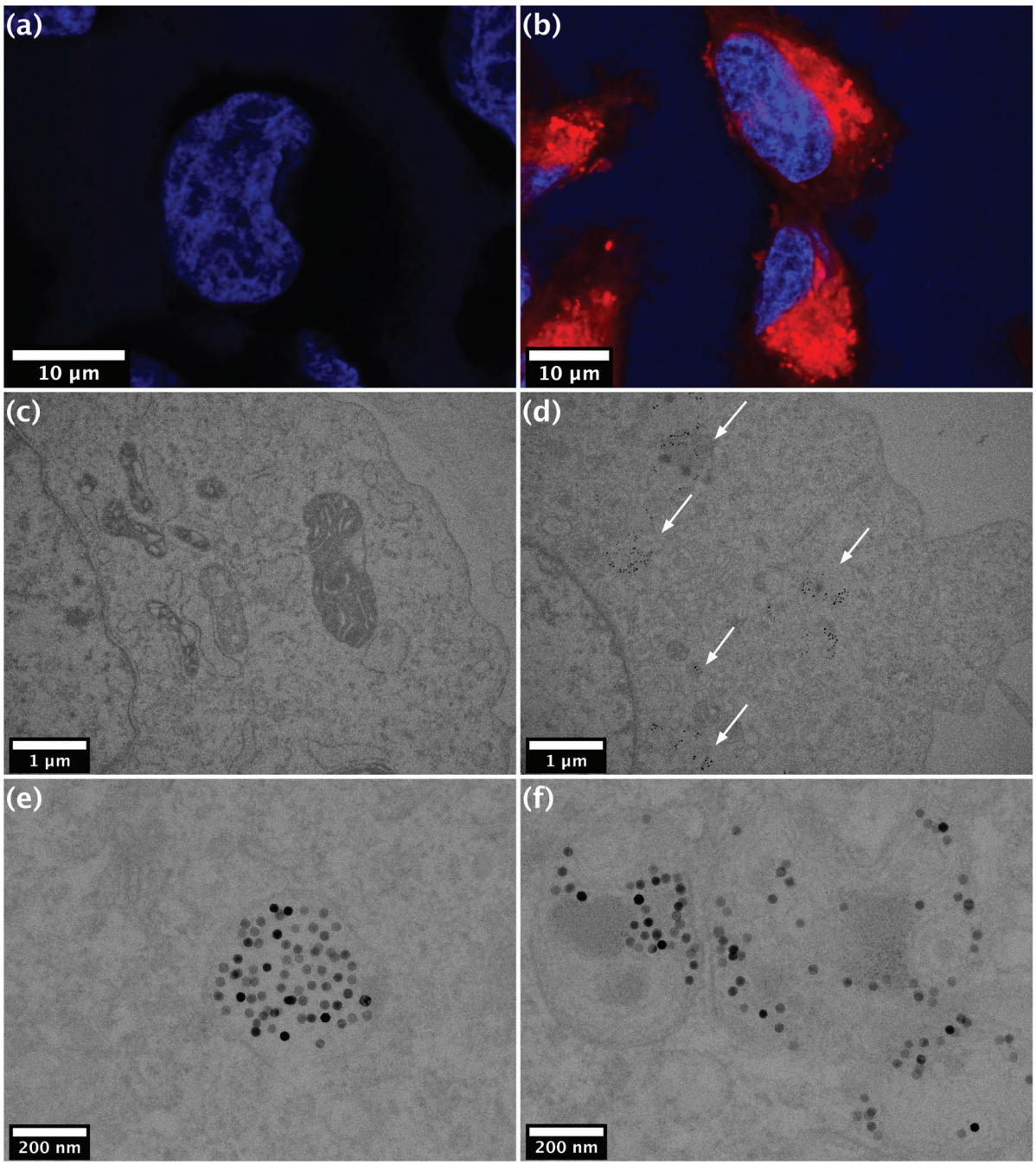

Fig. 2 Nanoparticle internalization observed before internalization of SPIONs, (a) and (c), and after, (b) and (d). Increasing detail of localization observed first through confocal fluorescence microscopy, (a)–(b), and then TEM, (c)–(d). Further magnified imaging by TEM confirms encapsulation of SPIONs in cytoplasmic vesicles including endosomes, (e), and lysosomes (f).

periods.[44] In addition, the coating protecting the nanoparticles plays a significant role in their stability over time with previous studies showing extensive biodegradation of nanoparticles coated with citric acid[45] and PEG.[46] Each of these possible circumstances is evaluated over relatively short periods (24 h) in the work presented here as the short-term fate is of primary interest.

TEM size analysis was performed using ImageJ software using a macro to outline the edges of particles and determine their diameter. This was done for as-synthesized and internalized SPIONs to assess if any decrease in size or change to size distribution occurred. Fig. 3a shows the two cases where there is no significant change and confirming that, over the incubation periods studied in this work, the physical dimensions

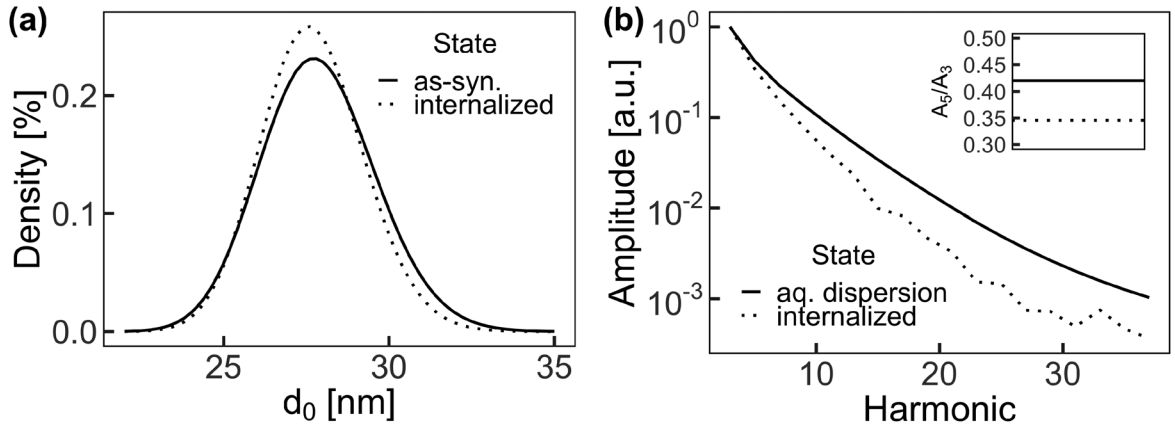

Fig. 3 Comparison of pre- and post-internalization core diameter size and size distribution (a), and MPS harmonic distribution (with inset A_5/A_3) (b). No significant difference observed for the SPION core physical dimensions while a reasonable decrease in harmonic amplitude is noted after internalization.

of the nanoparticles remain constant. This is likely attributed to the PMAO–PEG coating having sufficient thickness to prevent acidic species from readily diffusing to the nanoparticle core and allowing for acidic reactions. This is promising for SPION use in MPI as fate after injection into the body and internalization in cells is of crucial importance for short- and long-term clinical use.

Seeing no change in the physical characteristics and observing no obvious reasons why magnetic characteristics would be affected, it is important to directly observe the MPS performance of SPIONs after internalization in cells. One of the three batches of SPIONs has thus been exposed to cells under the same conditions as were used to observe internalization through microscopic imaging. Here a noticeable change in magnetic performance is observed for internalized SPIONs measured in live epithelial cancer cells. This change from freely dispersed in water to internalized in cells, shown in Fig. 3b, is a noted decrease in the amplitude of harmonics greater than the 1st and a 20% decrease in the ratio of the 5th over 3rd harmonics, A_5/A_3.

As no change in core size and size distribution is observed, other potential mechanisms must be explored for deterioration in intracellular SPION magnetic performance. Looking to the mechanisms utilized by these nanoparticles to generate a signal, Néel and Brownian relaxation, it is possible to attribute changing magnetic performance to either or both the viscosity of the surrounding environment and effective anisotropy, arising from the interparticle interactions of the nanoparticles. The variation in how much these two conditions will affect performance is dependent on the contribution of each relaxation mechanism to the total signal. This changes with core size and size distribution with the exact contributions in the range of core sizes between 20 and 30 nm being not fully known. It is expected that as core size increases, the contribution of Brownian relaxation will increase.

In order to determine if a significant reduction in Brownian contribution has occurred, control solutions of varying viscosity were prepared from glycerol and deionized water. These solutions, ranging from 0 to 100 weight % glycerol, were mixed with solutions of SPIONs, controlling the mass of iron across all samples, and characterized by MPS. Direct comparison to exact viscosity values used in Monte Carlo simulations is accomplished through conversion of final weight % of glycerol to viscosity through experimentally derived numerical formulae.[47–49]

Fig. 4 clearly shows no change in the magnetic response of SPIONs as a function of increasing viscosity, for average core diameters between 20 and 30 nm. This is consistent with the non-linear Monte Carlo simulated response of SPIONs under

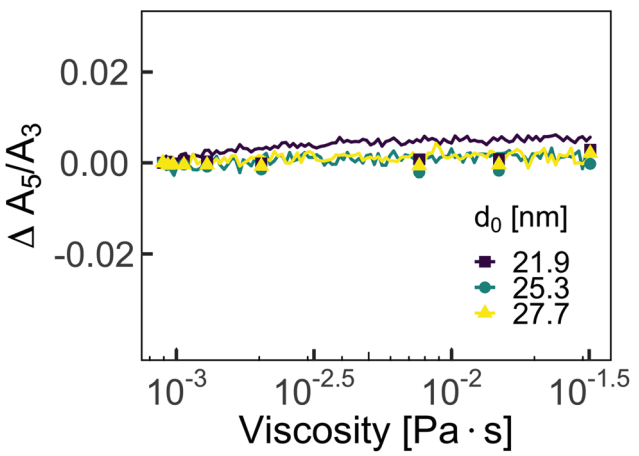

Fig. 4 Magnetic particle spectroscopy performance, A_5/A_3, as a function of solution viscosity of three different batches of SPIONs with increasing average diameters and approaching the optimal limit for Fe_3O_4 and γ-Fe_2O_3. Monte Carlo simulation results, shown as lines, of equivalent nanoparticle characteristics show consistent performance over expected range of viscosities.

identical conditions and suggests that over the range of viscosities studied, up to more than one order of magnitude greater than would be expected within a cell, there is no shift in magnetic response. In particular, the lack of decrease in A_5/A_3 suggests that the Brownian contribution to the magnetic performance of SPIONs with diameters between 20 and 30 nm is minimal. As viscosity only affects the Brownian component of magnetic nanoparticle relaxation, then it can further be said that viscosity should be ruled out as a contributing factor in the observed changes in the magnetic response of SPIONs with core diameters near those used in this work and internalized in cells.

With viscosity ruled out as a significant factor, it is necessary to address magnetostatic interactions of SPIONs for which the first step is further analysis by TEM. Specific characteristics of the sample preparation, including ultra-thin section thickness and well calibrated known pixel size of obtained images, allow for determination of interparticle separations in the projected image of a three-dimensional sample. Using ImageJ and python script analysis, two-dimensional interparticle separations have been tabulated, *Z*-separation equal to 0 nm in Fig. 5a. The range of possible three-dimensional interparticle separations has been estimated using the Pythagorean theorem where *Z*-separations are set at approximately equal intervals throughout the thickness of the ultra-thin resin sections. These are shown as *Z*-separation equal to 30, 50, and 70 nm in Fig. 5a. The averages of the minimum and maximum *Z*-separation histograms can be used as a range of the most likely interparticle separations. These average interparticle separations are used to compare dipole–dipole interaction energies to the thermal energy of the system, Fig. 5b. It is observed that the dipole–dipole energy of SPIONs in the size range in this work is expected to be significant and unable to be destabilized by random thermal energy, k_BT.

Based on the calculation of expected dipole–dipole energy of SPIONs, it is hypothesized that interparticle interactions, even without destabilization of surface coatings and direct aggregation, are the dominant contribution to decreased magnetic performance after internalization. To support this hypothesis, it is necessary to experimentally and theoretically observe nanoparticle magnetic performance under changing average interparticle separations. To control for interparticle separation experimentally, SPIONs have been dispersed in solutions of mannitol and deionized water with varying weight % of mannitol and lyophilized to control for relaxation mechanism as a variable. Increasing mannitol weight % has the effect of increasing physical bulk between nanoparticles on average and thus increasing their interparticle separations. Fig. 6a illustrates the performance of three different average core size SPIONs as a function of increasing mannitol weight %. Here it is noted that increasing average core size has the effect of significantly degrading magnetic performance as nanoparticles are allowed to associate and magnetostatically interact more closely. The largest core size of the three shows a greater than 80% reduction in A_5/A_3 while the next smallest only shows approximately a 20% reduction. The smallest of the three sizes shows no change in magnetic performance over the possible interparticle separations in this study suggesting that its dipole–dipole interaction energy is not significant until the particles are allowed much closer together.

Direct calculation of the interparticle separation is limited by the two-dimensional projection approximation and the experimental results, though broadly in agreement, are not entirely sufficient; thus the experimental results are also compared to Monte Carlo simulations. Fig. 6b illustrates supporting trends in SPION magnetic performance between approximately 40 to 60 nm center-to-center interparticle separations. This is a more detailed examination of the dipole–dipole interaction energy with non-linear dynamics and thus more realistic than the first principles approximation in Fig. 5b. Based on these results, it is concluded that the dipole–dipole interactions between SPIONs within cells are the dominant and sig-

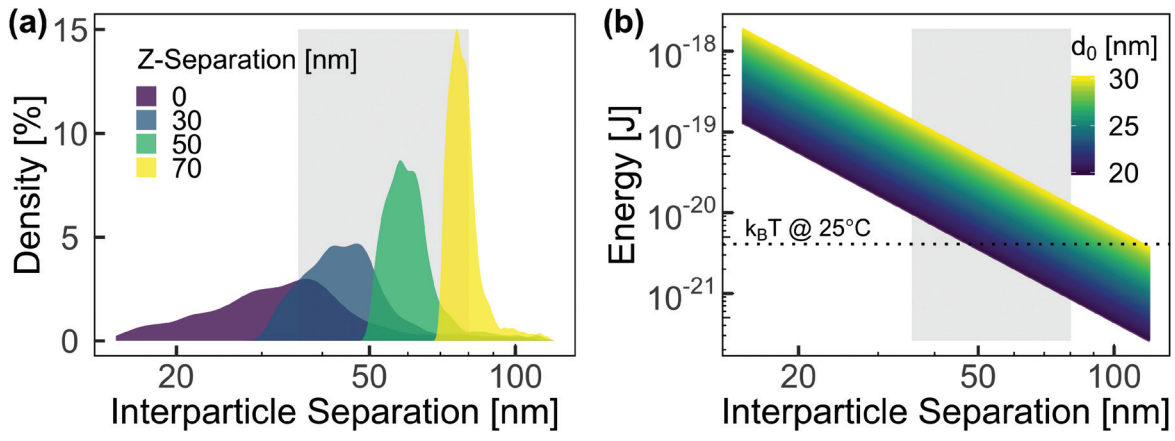

Fig. 5 Direct two-dimensional and estimation of three-dimensional interparticle separations as observed by TEM (a). The gray region highlights the range interparticle separations possible within the constraint of ultra-thin section thickness as a maximum *Z*-separation. Dipole–dipole interaction energies are compared to random thermal energy, k_BT, over the extracted range of interparticle separations (b). The dipole–dipole interaction energy is notably higher than random thermal energy over most of this range.

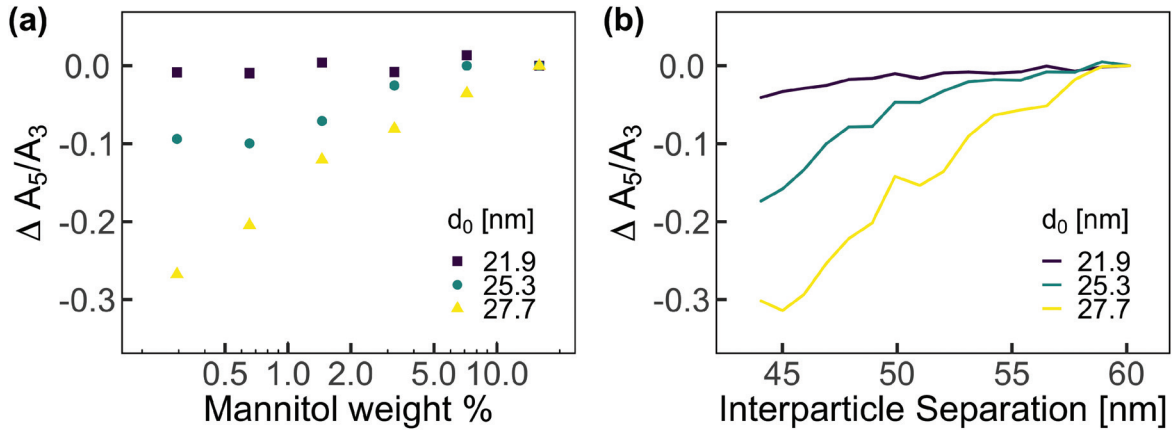

Fig. 6 Magnetic particle spectroscopy performance, A_5/A_3, as a function of mannitol weight % (a) and theoretical interparticle separation (b) of three different batches of SPIONs with increasing average core diameters. As before, Monte Carlo simulations support experimental trends over observed interparticle separations.

nificant contributor to changing magnetic performance. The latter is a crucial point for which Magnetic Particle Imaging characteristics of SPIONs must be optimized. It is now understood that increasing interparticle separations before and after internalization will lead to an overall improved magnetic performance in MPI and potentially in other diagnostic and treatment regimes such as magnetic fluid hyperthermia.

Conclusions

This work includes an investigation of SPION localization and dynamics after internalization in cells. Decreasing magnetic performance is explored through three routes, changing physical characteristics, changing the surrounding environment, and magnetic dipole–dipole interactions between nanoparticles in close proximity. Physical changes to the nanoparticle cores are ruled out through careful TEM size and size distribution analysis of nanoparticles before and after cell internalization. The effects of the surrounding environmental parameters, in particular the viscosity, on magnetic performance are experimentally and theoretically observed, but shown to be insignificantly affecting relaxation dynamics. Magnetostatic or dipole–dipole interactions of SPIONs, with optimal or near-optimal physical and crystallographic properties, are observed to affect performance significantly. Experimental and theoretical observations support the assumption that nanoparticles in this size range are expected to interact with one another and limit their ability to interact with an applied magnetic field. These results are of interest to the magnetic particle community, in particular, Magnetic Particle Imaging, where the imaging quality *in vivo* and after cellular internalization is key to advancing the technique to clinical settings. It is expected that increasing the amount of steric bulk, or coating material, on the surface of SPIONs will increase average interparticle separation, decrease magnetostatic interactions, and limit some or all of the loss in performance after internalization. Optimization of these coatings would advance the possibilities of short- and long-term applications which rely on magnetic signals. Such work is in progress in our laboratory.

Conflicts of interest

There are no conflicts to declare.

Acknowledgements

This work was supported by NIH Grant no. 5R03EB024819-02. The TEM work, supported by the Department of Energy, Office of Biological and Environmental Research, Molecules to Mesoscale Bioimaging project no. 66382, was performed using Environmental Molecular Sciences Laboratory, a national scientific user facility sponsored by the DOE OBER and located at Pacific Northwest National Laboratory. C. S. was supported by NSF Grant no. DGE-1256082.

References

1 T. F. Massoud and S. S. Gambhir, *Genes Dev.*, 2003, **17**, 545–580.
2 M. Ferrari, *Nat. Rev. Cancer*, 2005, **5**, 161–171.
3 P. K. Nguyen, J. Riegler and J. C. Wu, *Cell Stem Cell*, 2014, **14**, 431–444.
4 B. Gleich and J. Weizenecker, *Nature*, 2005, **435**, 1214–1217.
5 P. Ludewig, N. Gdaniec, J. Sedlacik, N. D. Forkert, P. Szwargulski, M. Graeser, G. Adam, M. G. Kaul, K. M. Krishnan, R. M. Ferguson, A. P. Khandhar, P. Walczak, J. Fiehler, G. Thomalla, C. Gerloff, T. Knopp and T. Magnus, *ACS Nano*, 2017, **11**, 10480–10488.

6 E. Y. Yu, M. Bishop, B. Zheng, R. M. Ferguson, A. P. Khandhar, S. J. Kemp, K. M. Krishnan, P. W. Goodwill and S. M. Conolly, *Nano Lett.*, 2017, **17**, 1648–1654.
7 B. Zheng, T. Vazin, P. W. Goodwill, A. Conway, A. Verma, E. Ulku Saritas, D. Schaffer and S. M. Conolly, *Sci. Rep.*, 2015, **5**, 14055.
8 J. W. M. Bulte, P. Walczak, M. Janowski, K. M. Krishnan, H. Arami, A. Halkola, B. Gleich and J. Rahmer, *Tomography*, 2015, **1**, 91–97.
9 E. Y. Yu, P. Chandrasekharan, R. Berzon, Z. W. Tay, X. Y. Zhou, A. P. Khandhar, R. M. Ferguson, S. J. Kemp, B. Zheng, P. W. Goodwill, M. F. Wendland, K. M. Krishnan, S. Behr, J. Carter and S. M. Conolly, *ACS Nano*, 2017, **11**, 12067–12076.
10 J. Weizenecker, B. Gleich, J. Rahmer, H. Dahnke and J. Borgert, *Phys. Med. Biol.*, 2009, **54**, L1–L10.
11 P. W. Goodwill, E. U. Saritas, L. R. Croft, T. N. Kim, K. M. Krishnan, D. V. Schaffer and S. M. Conolly, *Adv. Mater.*, 2012, **24**, 3870–3877.
12 A. P. Khandhar, P. Keselman, S. J. Kemp, R. M. Ferguson, P. W. Goodwill, S. M. Conolly and K. M. Krishnan, *Nanoscale*, 2017, **9**, 1299–1306.
13 K. M. Krishnan, *Fundamentals and Applications of Magnetic Materials*, Oxford University Press, 2016.
14 S. A. Shah, D. B. Reeves, R. M. Ferguson, J. B. Weaver and K. M. Krishnan, *Phys. Rev. B: Condens. Matter Mater. Phys.*, 2015, **92**, 094438.
15 B. Zheng, K. Lu, J. J. Konkle, D. W. Hensley, P. Keselman, R. D. Orendorff, Z. W. Tay, E. Yu, X. Y. Zhou, M. Bishop, B. Gunel, L. Taylor, R. M. Ferguson, A. P. Khandhar, S. J. Kemp, K. M. Krishnan, P. W. Goodwill and S. M. Conolly, in *Des. Appl. Nanoparticles Biomed. Imaging*, Springer International Publishing, Cham, 2017, pp. 69–93.
16 M. Graeser, T. Knopp, P. Szwargulski, T. Friedrich, A. von Gladiss, M. Kaul, K. M. Krishnan, H. Ittrich, G. Adam and T. M. Buzug, *Sci. Rep.*, 2017, **7**, 6872.
17 J. Haegele, K. Lüdtke-Buzug, C. Schaecke, M. Gräser, R. L. Duschka, N. Panagiotopoulos, T. M. Buzug, F. Vogt and J. Barkhausen, *Int. J. Nanomed.*, 2014, **9**, 4203.
18 R. M. Ferguson, A. P. Khandhar, S. J. Kemp, H. Arami, E. U. Saritas, L. R. Croft, J. Konkle, P. W. Goodwill, A. Halkola, J. Rahmer, J. Borgert, S. M. Conolly and K. M. Krishnan, *IEEE Trans. Med. Imaging*, 2015, **34**, 1077–1084.
19 R. M. Ferguson, A. P. Khandhar, H. Arami, L. Hua, O. Hovorka and K. M. Krishnan, *Biomed. Tech. Eng.*, 2013, **58**, 493–507.
20 H. Arami, A. Khandhar, D. Liggitt and K. M. Krishnan, *Chem. Soc. Rev.*, 2015, **44**, 8576–8607.
21 S. J. Kemp, R. M. Ferguson, A. P. Khandhar and K. M. Krishnan, *RSC Adv.*, 2016, **6**, 77452–77464.
22 C. D. Walkey and W. C. W. Chan, *Chem. Soc. Rev.*, 2012, **41**, 2780–2799.
23 A. Vonarbourg, C. Passirani, P. Saulnier and J.-P. Benoit, *Biomaterials*, 2006, **27**, 4356–4373.
24 M. Lundqvist, J. Stigler, G. Elia, I. Lynch, T. Cedervall and K. A. Dawson, *Proc. Natl. Acad. Sci. U. S. A.*, 2008, **105**, 14265–14270.
25 A. Hill and C. K. Payne, *RSC Adv.*, 2014, **4**, 31735–31744.
26 D. Leckband and J. Israelachvili, *Q. Rev. Biophys.*, 2001, **34**, 105.
27 H. Maeda, H. Nakamura and J. Fang, *Adv. Drug Delivery Rev.*, 2013, **65**, 71–79.
28 H. Gao, W. Shi and L. B. Freund, *Proc. Natl. Acad. Sci. U. S. A.*, 2005, **102**, 9469–9474.
29 I. Canton and G. Battaglia, *Chem. Soc. Rev.*, 2012, **41**, 2718.
30 B. D. Grant and J. G. Donaldson, *Nat. Rev. Mol. Cell Biol.*, 2009, **10**, 597–608.
31 Z. Chu, S. Zhang, B. Zhang, C. Zhang, C.-Y. Fang, I. Rehor, P. Cigler, H.-C. Chang, G. Lin, R. Liu and Q. Li, *Sci. Rep.*, 2015, **4**, 4495.
32 G. Sahay, D. Y. Alakhova and A. V. Kabanov, *J. Controlled Release*, 2010, **145**, 182–195.
33 J. Park, K. An, Y. Hwang, J.-G. Park, H.-J. Noh, J.-Y. Kim, J.-H. Park, N.-M. Hwang and T. Hyeon, *Nat. Mater.*, 2004, **3**, 891–895.
34 T. Pellegrino, L. Manna, S. Kudera, T. Liedl, D. Koktysh, A. L. Rogach, S. Keller, J. Rädler, G. Natile and W. J. Parak, *Nano Lett.*, 2004, **4**, 703–707.
35 W. W. Yu, E. Chang, C. M. Sayes, R. Drezek and V. L. Colvin, *Nanotechnology*, 2006, **17**, 4483–4487.
36 R. M. Ferguson, A. P. Khandhar and K. M. Krishnan, *J. Appl. Phys.*, 2012, **111**, 07B318.
37 A. Einstein, *Investigations on the Theory of the Brownian Movement*, Courier Corp., New York, 1956.
38 L. Néel, *Ann. Geophys.*, 1949, **5**, 99–136.
39 C. Shasha, E. Teeman and K. M. Krishnan, *IEEE Magn. Lett.*, 2017, **8**, 1–5.
40 J. A. Mindell, *Annu. Rev. Physiol.*, 2012, **74**, 69–86.
41 M. Levy, N. Luciani, D. Alloyeau, D. Elgrabli, V. Deveaux, C. Pechoux, S. Chat, G. Wang, N. Vats, F. Gendron, C. Factor, S. Lotersztajn, A. Luciani, C. Wilhelm and F. Gazeau, *Biomaterials*, 2011, **32**, 3988–3999.
42 D. Eberbeck, F. Wiekhorst, S. Wagner and L. Trahms, *Appl. Phys. Lett.*, 2011, **98**, 182502.
43 H. Arami, R. M. Ferguson, A. P. Khandhar and K. M. Krishnan, *Med. Phys.*, 2013, **40**, 071904.
44 H. Arami and K. M. Krishnan, *J. Appl. Phys.*, 2014, **115**, 17B306.
45 F. Mazuel, A. Espinosa, N. Luciani, M. Reffay, R. Le Borgne, L. Motte, K. Desboeufs, A. Michel, T. Pellegrino, Y. Lalatonne and C. Wilhelm, *ACS Nano*, 2016, **10**, 7627–7638.
46 L. Lartigue, D. Alloyeau, J. Kolosnjaj-Tabi, Y. Javed, P. Guardia, A. Riedinger, C. Péchoux, T. Pellegrino, C. Wilhelm and F. Gazeau, *ACS Nano*, 2013, **7**, 3939–3952.
47 L. W. Bosart and A. O. Snoddy, *Ind. Eng. Chem.*, 1928, **20**, 1377–1379.
48 P. Linstrom and W. Mallard, *NIST standard reference database*, 2005.
49 N.-S. Cheng, *Ind. Eng. Chem. Res.*, 2008, **47**, 3285–3288.

